Absolute ion density measurements in the afterglow of an RF atmospheric pressure plasma jet

Jingkai Jiang and Peter J. Bruggeman\*

Department of Mechanical Engineering, University of Minnesota, 111 Church Street SE, Minneapolis

55414 Minnesota, United States of America

\*email: pbruggem@umn.edu

Abstract

Atmospheric pressure plasma jets (APPJs) can enable large fluxes of reactive species impinging on treated

substrates in many applications. The relative importance of ionic versus neutral reactive species fluxes

produced by APPJs is to date mainly deduced from modeling due to the challenge of measuring absolute

ion densities/fluxes. In this study, a calibration was performed to determine the absolute densities of cold

ions in the afterglow region of an RF-driven atmospheric pressure plasma jet (APPJ) in Ar + 1% O<sub>2</sub> by

molecular beam mass spectrometry. Positive ion densities were found to be about 3-4 orders of magnitudes

lower than the densities of the dominant reactive neutral species (O,  $O_2(a^1\Delta_g)$ ,  $O_3$ ) in the afterglow region

of the APPJ at a distance larger than 2 mm from the visible plasma plume. The results illustrate the ability

of molecular beam mass spectrometry to enable a quantitative evaluation of both neutral and ionic species

in many applications using APPJs.

Key words: absolute ion density, APPJ, molecular beam mass spectrometer

1. Introduction

Atmospheric pressure plasma jets (APPJs) are widely used in a broad range of plasma-enabled applications

such as plasma medicine [1],[2], plasma decontamination [3], environmental remediation [4], and materials

processing [5]. A key distinctive feature of APPJs is that it enables the treatment of substrates both with

and without the plasma in direct contact with the substrate [6]. When the substrate is not in direct contact

with the plasma, the treatment is enabled by reactive species including neutral and ionic species produced

by APPJs that are convectively transported to the substrate. The high collisionality of ions at atmospheric

pressure does not lead to large ion energies near substrates as in low-pressure plasmas [7]. Nonetheless,

many ions have ionization energies in excess of typical bond energies of molecules [8] and hence ions can,

in addition to charging, still induce chemical reactions on substrates.

In spite that the absolute densities of ions were predicted to be significantly lower than neutral radicals in

the effluents of APPJs by models for indirect treatments [9],[10], ion-induced effects can a priori not always

be neglected. For example, the mass accommodation coefficient of an ion which describes the probability

1

of species entering the liquid is often assumed to be close to 1 [11], while neutral species have typical mass accommodation coefficients between 0.01 and 0.3 [12]. In this case, the ion flux across the gas-liquid interface might be comparable to neutral fluxes despite a 2 orders of magnitude lower impinging flux. In addition, the energy released by the exothermic charge recombination reaction can be significantly larger than that from radicals and accelerate surface reactions.

To quantitatively evaluate the role of different species in plasma-surface interactions, the absolute densities of neutral reactive species in the afterglow region of APPJs have been extensively characterized by a variety of diagnostics [13]–[17]. Nevertheless, the equivalent measurement of ionic species in atmospheric pressure plasmas is to date largely not quantitative [18]. It remains however extremely valuable to be able to measure the ratio of neutral reactive species and ion fluxes/densities for mechanistic studies of plasma-surface interactions. Molecular beam mass spectrometry is able to detect both neutral and ions at atmospheric pressure plasma [17]. While an extensive list of calibration approaches have been reported for neutral species [19]–[22], an equivalent effort for ion fluxes/densities remains subject of further investigation.

At low pressures and when the mean free path is larger than the sampling orifice, molecular beam mass spectrometer (MBMS) signals represent a measurement of species fluxes [23]. At atmospheric pressure, the mean free path is typically much smaller than the MBMS sampling orifice and hence in this collisional environment the velocity component of species is random and the MBMS signal is representative of the species density [24]. While this will be also applicable for ionic species, the presence of (strong) electric fields can impact the sampling and complicate a quantitative analysis of the mass spectrometer measurements.

In the field of combustion, the ion concentrations in a flame were previously calibrated using MBMS by adding metal salt solutions with known concentrations to the flame. As the temperature of the flame was over 2300 K, the metal was completely ionized and hence the resulting mass spectrum could be quantified [25]. This approach cannot be applied to low-temperature plasmas because the ionization degree of the added salt might significantly vary with plasma conditions in addition to have a huge impact on plasma properties. Große-Kreul et al. [18] investigated the sampling of ions at atmospheric pressure by MBMS through simulations of the MBMS system. A relation between the measured ion signal and the ion density was achieved via the theoretical determination of the ion transmission function of the mass spectrometer system. This led to an estimation of the ion density in the afterglow of RF He-APPJ of approximately  $5 \times 10^{15}$  m<sup>-3</sup>. While this approach provides a valuable estimate of the ion density, it does not replace an absolute calibration of the MBMS that also inherently considers the impact of instrument imperfections on the measurement.

In this work, we adopted the MBMS to measure the ionic species in the afterglow region of an RF-driven APPJ in Ar +1 %  $O_2$ . A calibration approach for ion measurements by MBMS was implemented using a corona discharge. Absolute densities of positive ions were compared with densities of the dominant neutral reactive species (O,  $O_2(a^1\Delta_g)$ ,  $O_3$ ). We limit ourselves in this work to corona discharges and the effluent of APPJs and exclude sampling through a sheath structure in the presence of a high electric field with possible large electric field gradients on the length scales of the sampling orifice diameter.

# 2. Experimental setup

# 2.1 Molecular beam mass spectrometer

Figure 1(a) shows the MBMS system used to measure ionic and neutral species in the APPJ effluent in this work. The MBMS consists of three vacuum stages, separated by skimmers, which enable to reduce the pressure from atmospheric pressure to  $\sim 10^{-7}$  Torr commensurate with the pressure required for the operation of the mass spectrometer (MS). The diameter of the sampling orifice of the MBMS at the atmospheric pressure side is 30  $\mu$ m and is embedded in a grounded stainless-steel sampling plate. The MS used was an EPIC 300 (Hiden Analytical Ltd). More details about the MBMS system can be found in [26].

The secondary ion mass spectrometry (SIMS) mode of the mass spectrometer was used to detect the ionic species, and bias voltages were applied on the two skimmers (-11 V and -41 V, respectively) separating the different pressure stages to guide the ions into the entrance of the mass spectrometer. The charged species in the molecular beam were focused by the ion optics (electrostatic lens) installed in front of the ionizer and pass through the energy filter (Bessel box) before reaching the mass analyzer and the detector. In addition, the measurement and calibration methods of O,  $O_2(a^1\Delta_g)$  and  $O_3$  were previously reported [22],[26].

#### 2.2 Plasma source

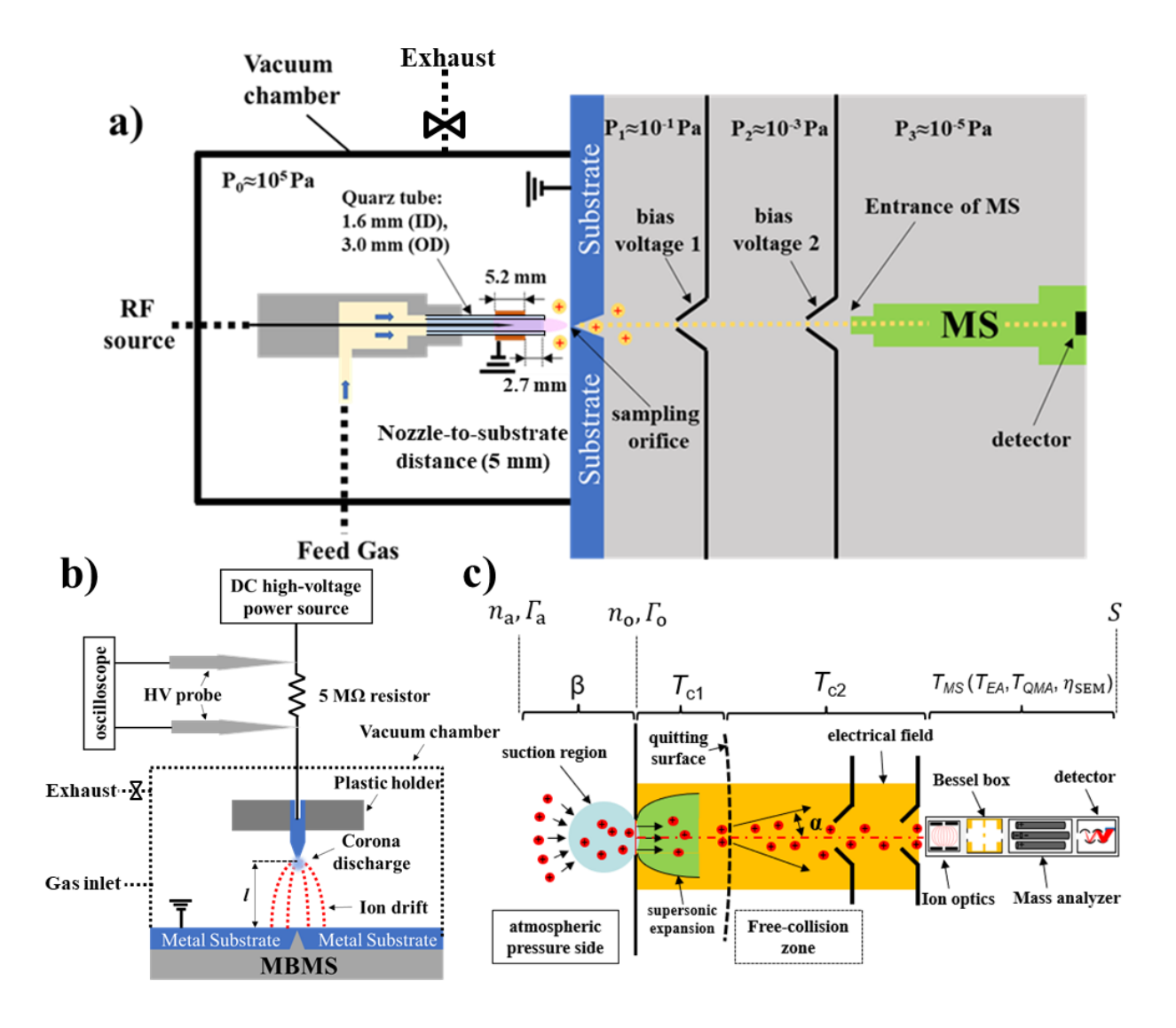


**Figure 1**. (a) Schematic of the MBMS system and the APPJ; (b) Schematic of the pin-to-plate corona discharge setup used for the absolute calibration of the ion measurement; (c) Illustration of the ion trajectory from the sampling at atmospheric pressure to the detector. The parameters in the figure are defined in the text.

The plasma jet used in this study is shown in Figure 1(a) and is identical to the APPJ described in [22]. The APPJ consists of a tungsten needle electrode, a cylindrical quartz tube, and a copper ring ground electrode. The inner and outer diameters of the quartz tube were 1.6 mm and 3 mm, respectively. The distance between the ring electrode to the nozzle of the quartz tube was fixed at 2.7 mm in this study. The plasma jet was driven by a radiofrequency (RF) sinusoidal wave at a frequency of 11.8 MHz modulated by 20% duty cycle (on – off modulation) at a frequency of 20 kHz. The modulation of the RF waveform enables a reduction

of the gas temperature while maintaining large radical densities [27]. The plasma dissipated power was obtained by multiplying the measured current and voltage waveforms as described in detail elsewhere [28]. The gas flow rate through the APPJ was kept constant at 0.2 standard liters per minute throughout the work. The gas temperature at the sampling plate was measured to be ~330 K by time-resolved measurements of Ar with electron energy of the ionizer set at 70 eV [29].

In this study, the plasma jet was placed in a vacuum chamber, operating in a homogenous Ar+1%  $O_2$  environment. The controlled environment was obtained by pumping down the chamber to 0.1 Torr twice and refilling it each time up to atmospheric pressure. The nitrogen impurity of the controlled gas environment was measured to be ~12 ppm using the residual gas analysis (RGA) mode of the mass spectrometry. In this manuscript, all the results of ionic species associated with APPJs were obtained in the far afterglow region (at least 2 mm from the visible tip of the plasma plume) of the plasma jet.

#### 3. Absolute ion density calibration

The absolute calibration of ion densities measured from the APPJ requires a reference ion source with a known absolute ion density or flux. We used a pin-to-plate corona discharge setup powered by a positive DC high-voltage sources (0-10 kV) for this purpose. Figure 1 (b) shows the schematic of the pin-to-plate corona discharge installed inside the vacuum chamber. The grounded stainless-steel sampling plate of the MBMS served as the plate electrode of the corona discharge. A 5 M $\Omega$  ballast resistor was inserted between the power supply and the corona needle and high-voltages probes (Tektronix P6015A) were used to measure the mean voltage drop across this resistor to obtain the mean discharge current. The maximum impact of the current pulses to dc corona discharge current was at most 10%, confirmed by operating the corona discharge with a different grounded electrode that allowed measuring the current pulses at the low voltage side using a voltage probe (Teledyne Lecroy PP016) with a large frequency bandwidth. Warburg's law [30] represents the spatial distribution of the current density in a corona discharge and hence the (undisturbed) local current density at the sampling orifice can be determined. As we focus in this study on the positive ions in the far afterglow of an APPJ operating in Ar + 1% O<sub>2</sub>, the corona discharge was operated in the same gas.

Figure 1(c) illustrates the ion motion from the atmospheric pressure side to the MBMS. The suction region marked in Figure 1(c) represents the distorted sampling region due to the existence of the sampling orifice. Knuth [31] previously reported that an MBMS measures an undistorted neutral density at a certain distance  $\delta$  in front of the substrate. The distance  $\delta$  for neutrals was previously reported to be about 2-5 orifice diameters [32],[33] and can be calculated as follows [31]:

$$\frac{\delta}{d} = 0.19\sqrt{\text{Re} \cdot \text{Sc}},\tag{1}$$

with Re the Reynolds number, Sc the Schmidt number, and d the diameter of the sampling orifice. In the case of ions, the presence of an electric field near the substrate can impact the motion of ions as the drift velocity  $(V_d)$  can be different than the gas velocity. Therefore, the suction region of ions might differ from that of neutral species.

The total mass spectrometer signal (S) can be related to the undistorted ion flux at the edge of the suction region ( $\Gamma_a$ ) can be written as follows (see also Figure 1(c)):

$$S = \Gamma_{a} \beta A_{0} T_{c1}(m_{i}) T_{c2}(m_{i}) T_{OMA}(m_{i}) T_{EA}(E_{i}) \eta_{SEM}(m_{i}, E_{i}), \tag{2}$$

 $\beta$  is defined as a sampling geometrical factor equal to the ratio of  $\Gamma_0/\Gamma_a$  in which  $\Gamma_0$  denotes the ion flux at the sampling orifice. A<sub>0</sub> is the area of the sampling orifice [34]. The total number of an ionic species being sampled can be given by the flux  $\Gamma_0$  multiplied with the sampling orifice area A<sub>0</sub>.  $T_{c1}$  and  $T_{c2}$  are the ion transmission efficiencies between the sampling orifice to the quitting surface (collisional zone), and between the quitting surface to the entrance of the MS (free-collision zone), respectively. The total ion transmission efficiency inside the MS is the product of the ion transmission efficiency inside the energy analyzer ( $T_{EA}$ ), the ion transmission efficiency inside the mass analyzer ( $T_{QMA}$ ), and the efficiency of the detector ( $\eta_{SEM}$ ) determined by the secondary electron generation at the multiplier. Equation 2 is valid for both the corona discharge and the APPJ although some factors in the right hand side of the equation are different for both cases as will be described below.

Considering that we measure the ions in the far afterglow region (>2 mm from the tip of plasma plume) of the APPJ, the majority of the electrons will have recombined before the effluent reaches the sampling location and no sheath is present between the plasma plume and the sampling plate [29]. Hence, the space charge and electric field are small in the plasma jet effluent and the electric field near the substrate is small and ion motion is mainly due to convection in the jet effluent. In this case the ion density relates to the ion flux at the sampling orifice as follows ( $\Gamma_0 = n_0 v_{sound}$ ,  $n_0$  the ion number density at the orifice) as the velocity at the orifice is in good approximation equal to the sound velocity because the pressure ratio of atmospheric pressure and the pressure in the first pressure reduction stage exceeds the critical pressure ratio and satisfies the sonic nozzle condition [17]. In addition, when the gas composition is not altered between the boundary of the suction zone and the sampling orifice in APPJs, the ion number density at the orifice  $n_0$  scales with the gas density  $\rho$  and can be linked to the undisturbed density  $n_0$  using the properties of an isentropic expansion [35]:

$$\frac{\mathrm{d}p}{p} = \gamma \frac{\mathrm{d}\rho}{\rho},\tag{3}$$

where p denotes the gas pressure, and  $\gamma$  the specific heat ratio of the gas. The conservation of momentum provides the relationship between p and  $\rho$  [35]:

$$\rho v dv = -dp, \tag{4}$$

Assuming that the velocity at the boundary of the suction zone is negligible compared to the sound velocity,  $n_a^{\text{tar}} \cong 1.6 n_0^{\text{tar}}$  is obtained after integrating eq. (3) and (4). The undisturbed ion density in APPJs can thus be obtained through the calibration as follows:

$$n_{\rm a}^{\rm tar} = \frac{1.6\beta^{\rm ref} \Gamma_{\rm a}^{\rm ref} S^{\rm tar}}{v_{\rm sound} S^{\rm ref}} \left( \frac{T_{\rm c1}^{\rm ref} T_{\rm c2}^{\rm ref} T_{\rm QMA}^{\rm ref} \eta_{\rm SEM}^{\rm ref}}{T_{\rm c1}^{\rm tar} T_{\rm c2}^{\rm tar} T_{\rm OMA}^{\rm tar} T_{\rm EA}^{\rm tar} \eta_{\rm SEM}^{\rm sem}} \right).$$
(5)

with the superscripts 'ref' and 'tar' the calibration measurement with the corona discharge and the targeted ion measurement in the APPJ, respectively.

Many of the ion transmission efficiencies including  $T_{c1}$ ,  $T_{c2}$ ,  $T_{QMA}$ ,  $T_{EA}$ ,  $\eta_{SEM}$  in eq. (2) can have an ion mass- or energy-dependence. The ion calibration should thus be performed with an ion with similar mass and energy. In addition, the possible difference between the transmission functions for the case of ions originating from the corona discharge and the APPJ needs to be assessed. The ion calibration procedure is outlined in the following sections and a simplified version of the calibration equation is developed.

## 3.1. The selection of calibration ion

The most dominant positive ion in the afterglow of Ar+1%  $O_2$  APPJs was found to be  $NO^+$  (30 amu) with a relative yield of more than 90%, as shown in Figure 2. This finding is consistent with the results published in [29].  $NO^+$  formation is due to the presence of traces of  $N_2$  in the feed gas.  $NO^+$  can be produced in charge transfer reactions between the primary ion  $O_2^+$  with NO [36]:

$$O_2^+ + NO \to O_2 + NO^+.$$
 (R1)

Hence NO<sup>+</sup> is the targeted positive ion that requires calibration.

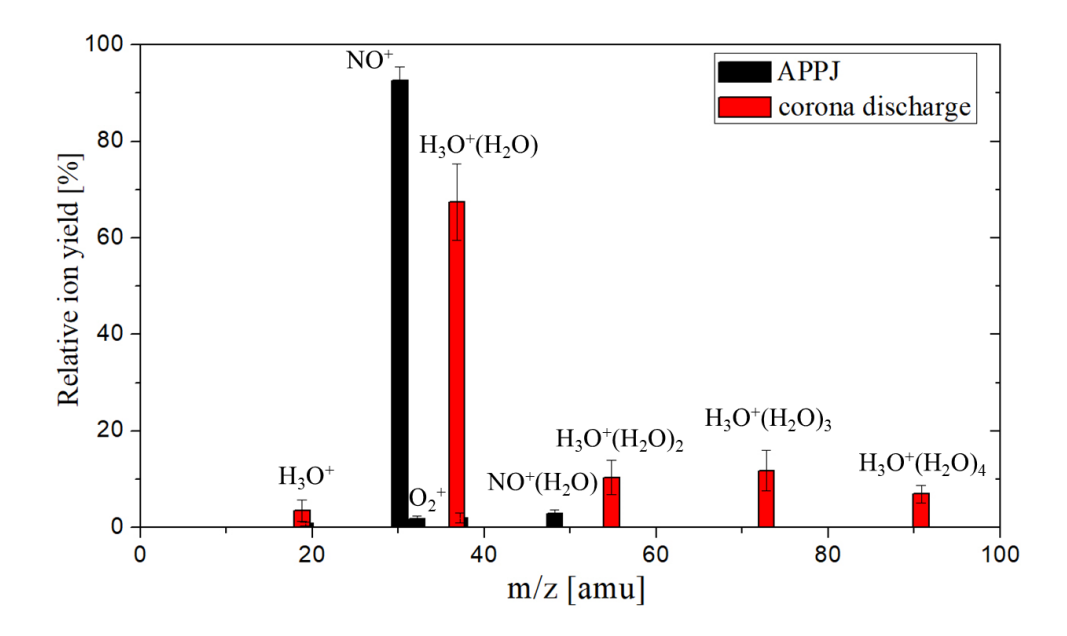


Figure 2. Relative positive ion yield in the Ar + 1% O<sub>2</sub> APPJ and corona discharge operating at 70 μA. For the APPJ, the nozzle-to-substrate distance is 5 mm, the gas flow rate is 0.2 slm and the dissipated plasma power is 2.3 W; for the corona discharge, the pin-to-plate distance is 15 mm. The error bars represent the standard deviation of the MS signals of multiple measurements.

Ideally, calibration with NO<sup>+</sup> should be pursued, but unfortunately, it is challenging to control the ion composition of the corona discharge. Figure 2 also shows an example of the relative ion yield in the Ar + 1% O<sub>2</sub> positive corona discharge detected at a pin-to-substrate distance of 15 mm. The dominant ion groups are found to be H<sub>3</sub>O<sup>+</sup>(H<sub>2</sub>O)<sub>n</sub>, and the most dominant ion with a relative yield ~70% is H<sub>3</sub>O<sup>+</sup>(H<sub>2</sub>O) and has a similar mass (37 amu) as NO<sup>+</sup> (30 amu). The ion compositions of the corona discharge under other gas environments were investigated, but the results were very similar to the Ar+1% O<sub>2</sub> case. This is because the ion drift time in the corona discharge (~10 ms) is longer than compared to the gas residence time (~1 ms) for the jet and the ions in the corona are the terminal ions after numerous collisions. H<sub>3</sub>O<sup>+</sup>(H<sub>2</sub>O)<sub>n</sub> ions were also detected as the most abundant terminal ions in positive corona discharges in other studies [37], and are more stable than the NO<sup>+</sup>(H<sub>2</sub>O)<sub>n</sub> ions [10].

Hence,  $H_3O^+(H_2O)$  was selected as the reference calibration ion. The validation of using  $H_3O^+(H_2O)$  as a referenced ion and the resulting uncertainty of the calibration caused by the mass difference between  $H_3O^+(H_2O)$  and  $NO^+$  is analyzed in section 3.3 but first, the determination of the ion flux in the calibration measurement is described.

#### 3.2. Determination of the ion flux in the corona

In the positive corona discharge, the current at the surface of the plate is due to the positive ions. The current density  $(j_x)$  in the corona discharge for a pin-to-plate distance (d) at the plate electrode can be described by Warburg's law for a positive corona [30]:

$$j(x) = j_0 \cos^{4.82}(\arctan\frac{x}{d}), \arctan\frac{x}{d} \le 60^{\circ}, \tag{6}$$

where the subscript 0 represents the centerline position and x is the radial distance from the axis of symmetry. The current density for the position outside the validity zone of eq. (6) can be neglected as it contributes less than 3% to the total current [38]. The total current at the surface of the metal plate can be computed by integrating eq. (6):

$$I = \int 2\pi x j_x \, \mathrm{d}x \,. \tag{7}$$

Combining equation (6) and (7), we can determine  $\Gamma_a^{\text{ref}} = j_0 e^{-1}$  given the measured total current I and e is the elementary charge. Figure 3(a) shows the relative radial distribution of the ion fluxes as measured using the MBMS. The experimental ion fluxes match Warburg's law, validating the use of eq. (6) for the calibration.

Figure 3(b) shows the relation between the current density  $j_0$  (and  $\Gamma_a^{\rm ref}$ ) and the mass spectrometer signal. The current density was changed by varying the applied voltage. A linear relationship between ion fluxes and MS signals ( $\Gamma_a^{\rm ref} = k \cdot S^{\rm ref}$ ) was found and a linear fit yields a calibration factor (k) of (2.2±0.06)×10<sup>10</sup> cm<sup>-2</sup> s<sup>-1</sup> (counts/s)<sup>-1</sup>, which determines the ratio  $\Gamma_a^{\rm ref}$  over  $S^{\rm ref}$  in eq. (5).

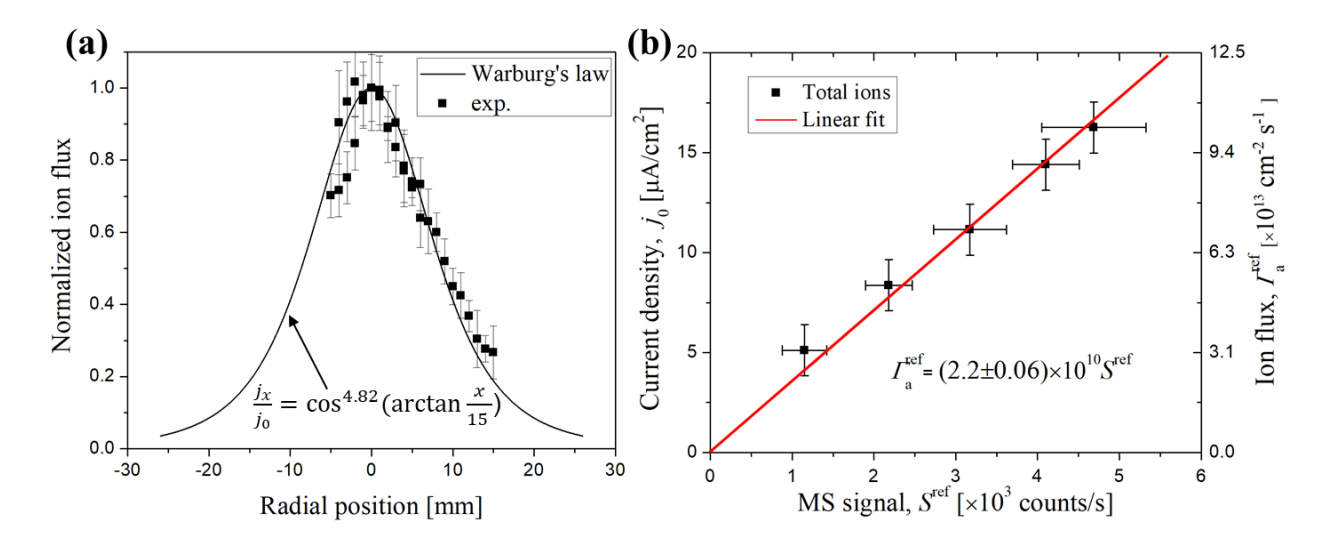


**Figure 3.** (a) Comparison of the radial distribution of the ion flux with Warburg's law for the positive corona discharge in Ar + 1%  $O_2$  operating at a current of 70  $\mu$ A; (b) Ion flux calibration curve obtained in Ar + 1% $O_2$  corona discharge for varying the current between 22  $\mu$ A and 70  $\mu$ A. The error bar of the

normalized ion flux in (a) and the error bar of the MS signal in (b) represent the standard deviation of the MS signals of multiple measurements; the error bar of the current density in (b) is determined by the resolution of the measurement.

# 3.3 Determination of geometrical factor and transmission efficiencies in the MBMS

## 3.3.1 Sampling at atmospheric pressure

As discussed earlier, the NO<sup>+</sup> ions in the afterglow of APPJs are thermalized and the ion velocity and energy are therefore the same as of neutral species. The energy and velocity of H<sub>3</sub>O<sup>+</sup>(H<sub>2</sub>O) in the corona discharge used for calibration requires further analysis. The Laplacian electric field at the substrate in the pin-to-plate corona discharge can be calculated from the formula available in [39]. However, the effect of space charge on the electric field at the cathode substrate cannot be neglected. The difference between the measured and Laplacian fields is particularly important for larger corona discharge current as used in this work [40]. In this work, we adopted the formula provided in [41],[42] yielding for estimating the electric field at the center point of cathode substrate:

$$E = \sqrt{\frac{4aBj}{\epsilon_0 \mu_i}},\tag{8}$$

where a is the focal distance, j the corona current density,  $\mu_i$  the ion mobility and B a parameter that is determined by the applied voltages as described in [41],[42]. The calculated electric fields are in the range of 1.9-3.9 kV/cm for voltages between 2.85-6.0 kV. This is about twice as the Laplacian electric fields (0.9-1.8 kV/cm). With typical ion mobilities in argon between 1.5 and 3.0 cm<sup>2</sup> V<sup>-1</sup> s<sup>-1</sup> [43], the ion drift velocity near the substrate is between 20~100 ms<sup>-1</sup>. This is significantly larger than the bulk gas velocity in the corona discharge as no external gas flow was applied and typical reported ionic wind velocities are ~1 ms<sup>-1</sup> in corona discharges [44]. This underlines the need to include ion drift in the analysis.

In APPJs, the suction region of ions should be the same as that of neutral species because ions are transported by convection. But for the corona discharge, the suction region of ions might be different from neutrals due to the drift velocity of the ions in the electric fields near the substrate ( $\sim 10^3$  V/cm). A simulation was performed in the boundary layer of the substrate ( $\sim 1$  mm) to estimate the value of  $\beta^{\rm ref}$  using the method described in [45]. The Laplace equation was solved for the electric potential, and Navier–Stokes equations for compressible and laminar flow were solved for the neutral gas flow. The migration of ions under the electrical field and their convective and diffusive transport was described by the following steady-state equation without considering reactions:

$$\nabla(-D\nabla n_{i} - Z\mu_{i}n_{i}\nabla V + n_{i}\vec{u}) = 0, \tag{9}$$

where  $n_i$  represents the ion density, D the diffusion coefficient, V the electrical potential, Z the charge, and  $\vec{u}$  the bulk gas velocity. The experimentally obtained current densities (ion fluxes) and zero diffusive ion fluxes are set as boundary conditions for the edge of the boundary layer and cathode plate, respectively. The estimated electric fields considering the effect of space charge and the ground potential were applied as the boundary conditions for the Laplace equation. The boundary conditions for the neutral gas flow used are identical as in [26]. Both cases with or without sampling through the orifice were investigated. The position of the undistorted ion flux at the edge of the suction region ( $\Gamma_a$ ) can be found by comparing the simulated ion flux distributions in these two cases. The ion flux at the orifice ( $\Gamma_o$ ) was obtained by the simulated result with sampling through the orifice. The simulated  $\beta^{\text{ref}}$  varies with the applied electric potentials of the corona discharge (2.85-6.0 kV), and the average  $\beta^{\text{ref}}$  is 5.8 with a maximum variation of 20%. This value is a factor 4-5 smaller compared to the case assuming a Laplacian electric field.

#### 3.3.2 MBMS ion transmission

The ion kinetic energy ( $KE_{ion}$ ) can be expressed by [46]:

$$KE_{\text{ion}} = \frac{m_{ion}v_d^2}{2} + \frac{M_b v_d^2}{2} + \frac{3k_B T}{2},\tag{10}$$

where  $m_{\text{ion}}$  is the mass of the ion, T is the gas temperature, and  $M_b$  is the mass of the gas (Ar). The first two terms in eq. (10) represent the drift energy due to the ion drift velocity in the field direction and to the random field energy due to ion velocity components randomized by elastic ion-neutral collisions [46]. The first two terms of eq. (10) are almost negligible to the thermal energy of ions (the third term) even when  $v_d$  is 100 m/s. Hence, we can conclude that the kinetic energy of sampled NO<sup>+</sup> in APPJs and its reference ion  $H_3O^+(H_2O)$  is in good approximation the same (~0.026 eV at 300 K).

After the ions enter the sampling orifice, they undergo a free-jet expansion with falling temperature and pressure and then enter the free-collision zone [18]. The chemical relaxation during the expansion in the molecular beam is typically not an issue for atmospheric pressure afterglow measurements due to the large collision frequency  $\sim 10^9$  s<sup>-1</sup> at atmospheric pressure [24]. The electrostatic field generated by the cones in the MBMS (see Figure 1 (a) and (c)) guide the ions during the expansion and reduce the ion losses significantly. As the ions enter the MBMS at the speed of sound and they all cross the same potential difference, the ions arriving at the mass spectrometer entrance have the same energy (but different velocities). The applied electrostatic fields, by the cones in the experiments, lead to ion velocities at the entrance of the MS that are 40 times higher than their initial velocity. Ion motions are therefore dominated by the electrostatic fields induced by the bias voltages on the skimmers. We confirmed this with an ion

energy scan of the Bessel box showing that the ions entering the MS have all the same energy independent of the ion mass.

Although ion motions are dominated by the electrostatic fields, the expansion can induce a radial velocity component of the sampled ions, as schematically shown in Figure 1(c). According to the simulation by Große-Kreul et al. [18], the expansion angle was within 5° immediately after the quitting surface. In the MBMS system used in our work, the electrostatic field guides charged particles and helps to limit the radial losses of ions in the supersonic expansion. A simulation was performed to capture the ion trajectories under the electrostatic fields in vacuum neglecting any collisions using the particle tracking module in COMSOL Multiphysics, which can help to evaluate the radial losses of ions. All geometric dimensions and bias voltages applied to the skimmers are specific for the used MBMS system design. In the model, charged particles were emitted at the sonic velocity from the orifice with a cone shape velocity distribution and then accelerated by the electrostatic fields inside the vacuum. The cone angle α was set at 5° and 15°, respectively. The results showed that ions with larger mass had larger radial losses nonetheless the radial losses between NO<sup>+</sup> and H<sub>3</sub>O<sup>+</sup>(H<sub>2</sub>O) were within 5% even for a cone angle of 15°. This means that the difference of  $T_{c2}$  for these two ions is within 5%. In addition, the total current in the circuit of the corona discharge is carried by ions with different mass, and the contribution of H<sub>3</sub>O<sup>+</sup>(H<sub>2</sub>O) is ~70%. Further assessing the  $T_{c2}$  for ions with different masses found in the corona discharge by the simulation, the uncertainty of the MS signals of the total ions is estimated to be at most 10%. In summary, the use of H<sub>3</sub>O<sup>+</sup>(H<sub>2</sub>O) as a calibration reference for NO<sup>+</sup> in our MBMS system will cause a total uncertainty of at most 15% in  $T_{c2}$ .

As all the ions enter the MS with the same energies,  $T_{\rm QMA}$  and  $T_{\rm EA}$  are the same for each ion. This was for  $T_{\rm QMA}$  experimentally confirmed in the ion mass range from 37 to 73 amu by showing that the optimized MS conditions are ion independent.  $T_{\rm QMA}$  was estimated to be unity for the same mass analyzer as used in this study by simulations reported in [18]. However, in the latter study, the optimized MS tuning parameters were reported to be energy-dependent which is not an issue for our study but should be considered when ions with a different mass entering the mass spectrometer have a different energy as in [15].

Additionally,  $\eta_{\text{SEM}}$  is the efficiency of the detector determined by the secondary electron generation at the multiplier.  $\eta_{\text{SEM}}$  is dependent on ion velocity and scales with  $m_{ion}^{-1/2}$  [17]. With the same MS settings,  $\eta_{\text{SEM}}$  might differ by 10% for NO<sup>+</sup> and H<sub>3</sub>O<sup>+</sup>(H<sub>2</sub>O). An additional 10% uncertainty could be present in the calibration due to the potential underestimation of ions with larger masses contributing to the current by mass-dependent  $\eta_{\text{SEM}}$ . However, this uncertainty will in good approximation be compensated by the inverse effect of  $T_{c2}$ .

In summary, the calibration of  $NO^+$  in the afterglow of an APPJ using a known ion flux of  $H_3O^+(H_2O)$  in a positive corona discharge based on the above analysis can be obtained by:

$$n_{\rm a}^{\rm tar} = \frac{1.6k \cdot \beta^{\rm ref} S^{\rm tar}}{v_{\rm sound}} = (6.3 \pm 2.1) \times 10^6 \cdot S^{\rm tar},$$
 (11)

# 4. Comparison of neutral and ionic species densities

The absolute density calibration of ions described in the previous section, allows us to compare the densities of neutral and ionic species in the effluent of the Ar + 1%  $O_2$  APPJ. Figure 4 shows the densities of different reactive species in the afterglow region as a function of plasma dissipated power at a fixed nozzle-to-substrate distance of 5 mm.  $O_2(a^1\Delta_g)$  is the dominant reactive species in the afterglow region with densities reaching  $10^{16}$  cm<sup>-3</sup>. O and  $O_3$  are the other two main reactive species with densities between  $10^{14}$  and  $10^{16}$  cm<sup>-3</sup>. The densities of the ions vary between  $\sim 10^9$ - $10^{12}$  cm<sup>-3</sup> in the power range of 1.4-2.6 W. A pseudo-1D plug flow model for the Ar plasma jet showed that the positive ion density near the tip of the plasma plume was on the order of  $\sim 10^{11}$  cm<sup>-3</sup> [10], which is one order of magnitude smaller than our measurements. In this plug flow model, the plasma was assumed to be homogenous leading to an underestimation of the ion density. The electron densities near the tip of the visible plasma plume of the same RF-driven APPJs but in Ar was experimentally measured to be  $\sim 10^{12}$ - $10^{13}$  cm<sup>-3</sup> [47]. This is similarly significantly larger than found in the plug flow model [10].

Increasing the plasma dissipated power increases the visible plasma plume length (approximately in the range of 1-3 mm in this study), hence the distance between the visible plasma region to the sampling orifice changes accordingly. This allows to obtain an estimate of the ion flux for near touching plasma conditions. Indeed, an extrapolation of the ion density with an exponential fitted line through the data points to 3 W, which corresponds to the power at which the plasma is in direct contact with the substrate at 5 mm nozzle-to-substrate distance, provides an estimation of the ion density at the visible plasma plume tip of ~3×10<sup>12</sup> cm<sup>-3</sup>, very similar to the measured electron densities near the tip of the visible plasma plume [47] and further supporting the validity of the ion calibration approach. There is unfortunately limited reported information on the densities of the charged species in the afterglow region of RF APPJs even from 2-dimensional fluid models, not allowing for more detailed validation of the absolute calibration approach.

In addition, a change in 2 mm of plume length leads to a change in gas residence time from the tip of the visible plasma plume to the sampling orifice of about ~1 ms. While species densities can vary with power within the visibly plume, the lifetime of the species can provide insights in their measured trends. O<sub>3</sub> is a long-lived species and hence its density does not change significantly on this time scale (Figure 4). Based on the dominant reactions reported in [22],[26], the lifetimes of O and  $O_2(a^1\Delta_g)$  in Ar+1%  $O_2$  environment

are estimated to be 2.5 ms and 13 ms, respectively. The obtained lifetimes are consistent with a much faster drop in the density of O compared to  $O_2(a^1\Delta_g)$  with decreasing plasma power. The dominant loss mechanism of ions in the afterglow region, depleted from electrons, is the fast ion-ion recombination reaction, with a reaction rate coefficient of  $\sim 10^{-7}$  cm<sup>-3</sup> s<sup>-1</sup> [48]. The negative ion densities for the same experimental conditions are below the detection limit and their densities are assumed to be identical to those of positive ions in the afterglow region. This is not an inconsistent assumption as the ion sampling for positive and negative ions is optimal for different MBMS settings suggesting different sampling conditions and transmission efficiencies. In addition, typically a much broader range of different negative ions compared to positive is observed which reduces the individual negative ion signal [49]. The lifetime of ions for a positive and negative ion density of  $10^{12}$  cm<sup>-3</sup> is therefore two orders of magnitude smaller than the gas residence time ( $\sim 1$  ms), consistent with the fast decrease in ion densities with decreasing plasma power.

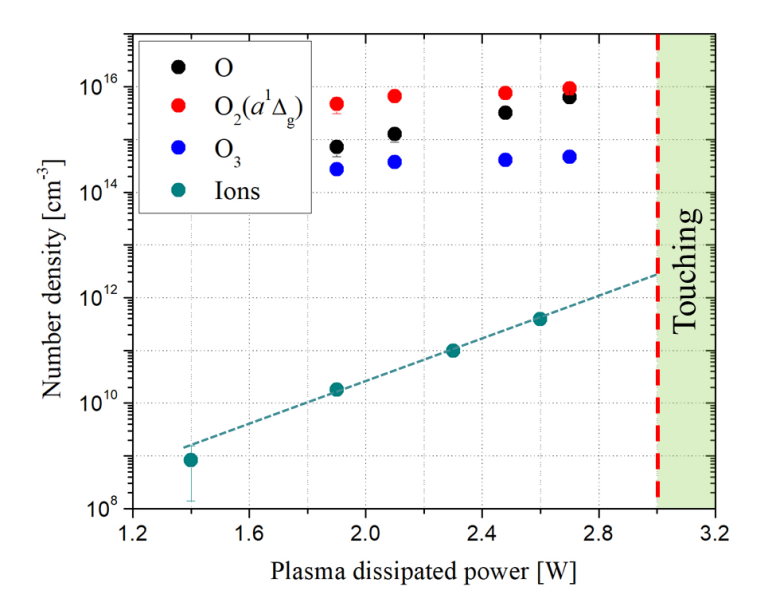


**Figure 4.** Densities of O,  $O_2(a^1\Delta_g)$ ,  $O_3$  and ions as a function of plasma dissipated power in the afterglow region of Ar + 1%  $O_2$  APPJs. The nozzle-to-substrate distance is fixed at 5 mm. The ion density is the density of  $NO^+$  with the exception of the 2.6 W case, for which the sum of  $NO^+$  and  $O_2^+$  is shown because of its higher relative yield. The error bars refer to the uncertainties of the MS signals in multiple measurements.

In conclusion, the ion density is three orders of magnitude lower than the dominant reactive neutral species  $(O_3, O \text{ and } O_2(a^1\Delta_g))$  in an RF-driven plasma jet for non-touching plasma conditions.

## 5. Conclusion

In this paper, a calibration approach was developed to enable the absolute density measurement of ionic species in the afterglow of an RF-driven APPJ by MBMS. A corona discharge generated in the same gas composition as the APPJ was used as the reference ion source. The sources of uncertainty in the calibration were analyzed. The densities of ions in the afterglow region of the APPJ were found to be about 3 orders of magnitudes lower than that of neutral species. The results illustrate the possibility to use MBMS to measure absolute ionic species densities in the afterglow region of APPJs. This might be of great importance for evaluating the role of ionic species in plasma-surface interactions. The complex processes in sampling at atmospheric pressure could impede the direct use of this calibration approach for ion sampling in atmospheric pressure plasma sheaths, requiring more complex modeling to illuminate and quantify ion sampling in collisional sheaths.

## Acknowledgment

This material is based upon work supported by the National Science Foundation (CBET 1703439) and the US Department of Energy, Office of Science, Office of Fusion Energy Sciences General Plasma Science program under award number DE-SC0020232 and DE-SC0001939. The authors would like to acknowledge the Minnesota Supercomputing Institute at the University of Minnesota for providing resources that contributed to the results reported in this work.

#### Reference

- [1] Bekeschus, S.; Schmidt, A.; Weltmann, K.-D.; von Woedtke, T. The Plasma Jet KINPen A Powerful Tool for Wound Healing. *Clin. Plasma Med.* **2016**, *4* (1), 19–28.
- [2] Athanasopoulos, D.; Svarnas, P.; Ladas, S.; Kennou, S.; Koutsoukos, P. On the Wetting Properties of Human Stratum Corneum Epidermidis Surface Exposed to Cold Atmospheric-Pressure Pulsed Plasma. *Appl. Phys. Lett.* **2018**, *112* (21), 213703.
- [3] Niemira, B. A. Cold Plasma Decontamination of Foods. *Annu. Rev. Food Sci. Technol.* **2012**, *3* (1), 125–142.
- [4] Foster, J.; Sommers, B. S.; Gucker, S. N.; Blankson, I. M.; Adamovsky, G. Perspectives on the Interaction of Plasmas With Liquid Water for Water Purification. *IEEE Trans. Plasma Sci.* **2012**, 40 (5), 1311–1323.
- [5] Penkov, O. V.; Khadem, M.; Lim, W.-S.; Kim, D.-E. A Review of Recent Applications of Atmospheric Pressure Plasma Jets for Materials Processing. *J. Coatings Technol. Res.* **2015**, *12* (2), 225–235.

- [6] Fridman, G.; Brooks, A. D.; Balasubramanian, M.; Fridman, A.; Gutsol, A.; Vasilets, V. N.; Ayan, H.; Friedman, G. Comparison of Direct and Indirect Effects of Non-Thermal Atmospheric-Pressure Plasma on Bacteria. *Plasma Process. Polym.* 2007, 4 (4), 370–375.
- [7] Oehrlein, G. S.; Hamaguchi, S. Foundations of Low-Temperature Plasma Enhanced Materials Synthesis and Etching. *Plasma Sources Sci. Technol.* **2018**, *27* (2), 023001.
- [8] Mehta, P.; Barboun, P.; Go, D. B.; Hicks, J. C.; Schneider, W. F. Catalysis Enabled by Plasma Activation of Strong Chemical Bonds: A Review. *ACS Energy Lett.* **2019**, *4* (5), 1115–1133.
- [9] Hemke, T.; Wollny, A.; Gebhardt, M.; Brinkmann, R. P.; Mussenbrock, T. Spatially Resolved Simulation of a Radio-Frequency Driven Micro-Atmospheric Pressure Plasma Jet and Its Effluent. *J. Phys. D. Appl. Phys.* **2011**, *44* (28), 285206.
- [10] Gaens, W. Van; Bogaerts, A. Kinetic Modelling for an Atmospheric Pressure Argon Plasma Jet in Humid Air. *J. Phys. D. Appl. Phys.* **2013**, *46* (27), 275201.
- [11] Tian, W.; Kushner, M. J. Atmospheric Pressure Dielectric Barrier Discharges Interacting with Liquid Covered Tissue. J. Phys. D. Appl. Phys. 2014, 47 (16), 165201.
- [12] Davidovits, P.; Kolb, C. E.; Williams, L. R.; Jayne, J. T.; Worsnop, D. R. Mass Accommodation and Chemical Reactions at Gas-Liquid Interfaces. *Chem. Rev.* **2006**, *106* (4), 1323–1354.
- [13] Zhang, S.; van Gaens, W.; van Gessel, B.; Hofmann, S.; van Veldhuizen, E.; Bogaerts, A.; Bruggeman, P. Spatially Resolved Ozone Densities and Gas Temperatures in a Time Modulated RF Driven Atmospheric Pressure Plasma Jet: An Analysis of the Production and Destruction Mechanisms. J. Phys. D. Appl. Phys. 2013, 46 (20), 205202.
- [14] Kondeti, V. S. S. K.; Phan, C. Q.; Wende, K.; Jablonowski, H.; Gangal, U.; Granick, J. L.; Hunter, R. C.; Bruggeman, P. J. Long-Lived and Short-Lived Reactive Species Produced by a Cold Atmospheric Pressure Plasma Jet for the Inactivation of Pseudomonas Aeruginosa and Staphylococcus Aureus. Free Radic. Biol. Med. 2018, 124 (October 2017), 275–287.
- [15] Sousa, J. S.; Niemi, K.; Cox, L. J.; Th Algwari, Q.; Gans, T. Cold Atmospheric Pressure Plasma Jets as Sources of Singlet Delta Oxygen for Biomedical Applications. *J. Appl. Phys* **2011**, *109*, 123302.
- [16] Engeln, R.; Klarenaar, B.; Guaitella, O. Foundations of Optical Diagnostics in Low-Temperature Plasmas. *Plasma Sources Sci. Technol.* **2020**, *29* (6), 063001.

- [17] Benedikt, J.; Hecimovic, A.; Ellerweg, D.; von Keudell, A. Quadrupole Mass Spectrometry of Reactive Plasmas. *J. Phys. D. Appl. Phys.* **2012**, *45* (40), 403001.
- [18] Große-Kreul, S.; Hübner, S.; Benedikt, J.; von Keudell, A. Sampling of Ions at Atmospheric Pressure: Ion Transmission and Ion Energy Studied by Simulation and Experiment. *Eur. Phys. J. D* **2016**, *70* (5), 103.
- [19] Ellerweg, D.; Benedikt, J.; von Keudell, A.; Knake, N.; Schulz-von der Gathen, V. Characterization of the Effluent of a He/O 2 Microscale Atmospheric Pressure Plasma Jet by Quantitative Molecular Beam Mass Spectrometry. *New J. Phys.* **2010**, *12* (1), 013021.
- [20] Willems, G.; Benedikt, J.; von Keudell, A. Absolutely Calibrated Mass Spectrometry Measurement of Reactive and Stable Plasma Chemistry Products in the Effluent of a He/H 2 O Atmospheric Plasma. *J. Phys. D. Appl. Phys.* **2017**, *50* (33), 335204.
- [21] Benedikt, J.; Ellerweg, D.; Schneider, S.; Rügner, K.; R, R.; Kersten, H.; Benter, T. Mass Spectrometry of Positive Ions and Neutral Species in the Effluent of an Atmospheric Pressure Plasma with Hexamethyldisiloxane and Oxygen. *J. Phys. D. Appl. Phys.* **2013**, *46* (46), 464017.
- [22] Jiang, J.; Gonzalvo, Y. A.; Bruggeman, P. J. Spatially Resolved Density Measurements of Singlet Delta Oxygen in a Non-Equilibrium Atmospheric Pressure Plasma Jet by Molecular Beam Mass Spectrometry. *Plasma Sources Sci. Technol.* **2020**, *29* (4), 045023.
- [23] Hamers, E. A. G.; van Sark, W. G. J. H. M.; Bezemer, J.; Goedheer, W. J.; van der Weg, W. F. On the Transmission Function of an Ion-Energy and Mass Spectrometer. *Int. J. Mass Spectrom. Ion Process.* **1998**, *173* (1–2), 91–98.
- [24] Große-Kreul, S.; Hübner, S.; Schneider, S.; Ellerweg, D.; von Keudell, A.; Matejčík, S.; Benedikt, J. Mass Spectrometry of Atmospheric Pressure Plasmas. *Plasma Sources Sci. Technol.* **2015**, *24* (4), 044008.
- [25] Hayhurst, A. N.; Telford, N. R. Mass Spectrometric Sampling of Ions from Atmospheric Pressure Flames—I: Characteristics and Calibration of the Sampling System. *Combust. Flame* **1977**, *28*, 67–80.
- [26] Jiang, J.; Luo, Y.; Moldgy, A.; Aranda Gonzalvo, Y.; Bruggeman, P. J. Absolute Spatially and Time-Resolved O, O<sub>3</sub>, and Air Densities in the Effluent of a Modulated RF-Driven Atmospheric Pressure Plasma Jet Obtained by Molecular Beam Mass Spectrometry. *Plasma Process. Polym.* **2019**, e1900163.

- [27] Hofmann, S.; van Gils, K.; van der Linden, S.; Iseni, S.; Bruggeman, P. Time and Spatial Resolved Optical and Electrical Characteristics of Continuous and Time Modulated RF Plasmas in Contact with Conductive and Dielectric Substrates. *Eur. Phys. J. D* **2014**, *68* (3), 56.
- [28] Hofmann, S.; van Gessel, A. F. H.; Verreycken, T.; Bruggeman, P. Power Dissipation, Gas Temperatures and Electron Densities of Cold Atmospheric Pressure Helium and Argon RF Plasma Jets. *Plasma Sources Sci. Technol.* **2011**, *20* (6), 065010.
- [29] Jiang, J.; Bruggeman, P. J. Spatially Resolved Absolute Densities of Reactive Species and Positive Ion Flux in He-O<sub>2</sub> RF-Driven Atmospheric Pressure Plasma Jet: Touching and Non-Touching with Dielectric Substrate. *J. Phys. D. Appl. Phys.* **2020**, *53* (28), 28LT01.
- [30] Jones, J. E.; Davies, M.; Goldman, A.; Goldman, M. A Simple Analytic Alternative to Warburg's Law. J. Phys. D. Appl. Phys. 1990, 23 (5), 542–552.
- [31] Knuth, E. L. Composition Distortion in MBMS Sampling. *Combust. Flame* **1995**, *103* (3), 171–180.
- [32] Biordi, J. C.; Lazzara, C. P.; Papp, J. F. Molecular Beam Mass Spectrometry Applied to Determining the Kinetics of Reactions in Flames. I. Empirical Characterization of Flame Perturbation by Molecular Beam Sampling Probes. *Combust. Flame* **1974**, *23* (1), 73–82.
- [33] CATTOLICA, R. J.; YOON, S.; KNUTH, E. L. OH Concentration in an Atmospheric-Pressure Methane-Air Flame from Molecular-Beam Mass Spectrometry and Laser-Absorption Spectroscopy. *Combust. Sci. Technol.* **1982**, *28* (5–6), 225–239.
- [34] Fenn, J. B. Mass Spectrometric Implications of High-Pressure Ion Sources. *Int. J. Mass Spectrom.* **2000**, *200* (1–3), 459–478.
- [35] Van Wylen, Gordon John, Richard Edwin Sonntag, and C. B. *Fundamentals of Classical Thermodynamics*; New York: Wiley, 1976.
- [36] Kossyi, I. A.; Kostinsky, A. Y.; Matveyev, A. A.; Silakov, V. P. Kinetic Scheme of the Non-Equilibrium Discharge in Nitrogen-Oxygen Mixtures. *Plasma Sources Sci. Technol.* **1992**, *I* (3), 207–220.
- [37] Sabo, M.; Klas, M.; Wang, H.; Huang, C.; Chu, Y.; Matejčík, Š. Positive Corona Discharge Ion Source with IMS/MS to Detect Impurities in High Purity Nitrogen. *Eur. Phys. J. Appl. Phys.* **2011**, 55 (1).
- [38] Adamiak, K.; Atten, P. Simulation of Corona Discharge in Point–Plane Configuration. J. Electrostat.

- **2004**, *61* (2), 85–98.
- [39] Fridman, Alexander, and L. A. K. Plasma Physics and Engineering; CRC press, 2004.
- [40] Cui, Y.; Zhuang, C.; Zeng, R. Electric Field Measurements under DC Corona Discharges in Ambient Air by Electric Field Induced Second Harmonic Generation. *Appl. Phys. Lett.* **2019**, *115* (24), 244101.
- [41] Fujita, H. 直流無パルス性正針コロナ場の簡便電界計算法. *IEEJ Trans. Fundam. Mater.* **1980**, 100 (6), 323–330.
- [42] Hidaka, K.; Fujita, H. A New Method of Electric Field Measurements in Corona Discharge Using Pockels Device. *J. Appl. Phys.* **1982**, *53* (9), 5999–6003.
- [43] Ellis, H. W.; McDaniel, E. W.; Albritton, D. L.; Viehland, L. A.; Lin, S. L.; Mason, E. A. Transport Properties of Gaseous Ions over a Wide Energy Range. Part II. *At. Data Nucl. Data Tables* **1978**, *22* (3), 179–217.
- [44] Robinson, M. Movement of Air in the Electric Wind of the Corona Discharge. *Trans. Am. Inst. Electr. Eng. Part I Commun. Electron.* **1961**, 80 (2), 143–150.
- [45] Wissdorf, W.; Pohler, L.; Klee, S.; Müller, D.; Benter, T. Simulation of Ion Motion at Atmospheric Pressure: Particle Tracing Versus Electrokinetic Flow. *J. Am. Soc. Mass Spectrom.* **2012**, *23* (2), 397–406.
- [46] Sieck, L. W.; Heron, J. T.; Green, D. S. Chemical Kinetics Database and Predictive Schemes for Humid Air Plasma Chemistry. Part I: Positive Ion–Molecule Reactions. *Plasma Chem. Plasma Process.* **2000**, *20* (2), 235–258.
- [47] van Gessel, B.; Brandenburg, R.; Bruggeman, P. Electron Properties and Air Mixing in Radio Frequency Driven Argon Plasma Jets at Atmospheric Pressure. *Appl. Phys. Lett.* **2013**, *103* (6), 064103.
- [48] Fridman, A. *Plasma Chemistry*; Cambridge University Press: Cambridge, 2008.
- [49] Van Gils, C. A. J.; Hofmann, S.; Boekema, B. K. H. L.; Brandenburg, R.; Bruggeman, P. J. Mechanisms of Bacterial Inactivation in the Liquid Phase Induced by a Remote RF Cold Atmospheric Pressure Plasma Jet. J. Phys. D. Appl. Phys. 2013, 46 (17).